Fourier transform imaging of impurities in the unit cells of crystals: Mn in GaAs

T.-L. Lee,[1,*] C. Bihler,[2] W. Schoch,[3] W. Limmer,[3] J. Daeubler,[3] S. Thieß,[1,4] M. S. Brandt,[2] and J. Zegenhagen[1]
[1]*European Synchrotron Radiation Facility, BP 220, F-38043 Grenoble Cedex 9, France*
[2]*Walter Schottky Institut, Technische Universität München, Am Coulombwall 3, D-85748 Garching, Germany*
[3]*Institut für Halbleiterphysik, Universität Ulm, D-89069 Ulm, Germany*
[4]*Institut für Experimentalphysik, Universität Hamburg, Luruper Chaussee 149, D-22761 Hamburg, Germany*
(Received 12 December 2009; revised manuscript received 24 May 2010; published 9 June 2010)

The lattice sites of Mn in ferromagnetic (Ga,Mn)As thin films were imaged using the x-ray standing wave technique. The model-free images, obtained straightforwardly by Fourier inversion, disclose immediately that the Mn mostly substitutes the Ga with a small fraction residing on minority sites. The images further reveal variations in the Mn concentrations of the different sites upon post-growth treatments. Subsequent model refinement based on the directly reconstructed images resolves with high precision the complete Mn site distributions. It is found that post-growth annealing increases the fraction of substitutional Mn at the expense of interstitial Mn whereas hydrogenation has little influence on the Mn site distribution. Our study offers an element-specific high-resolution imaging approach for accurately determining the detailed site distributions of dilute concentrations of atoms in crystals.

DOI: 10.1103/PhysRevB.81.235207 PACS number(s): 68.49.Uv, 68.37.Yz, 68.55.Ln, 75.50.Pp

I. INTRODUCTION

In studying highly charge-compensated materials, such as ZnO,[1] GaN,[2] and dilute magnetic semiconductors (DMS),[3] where a dopant element may occupy multiple lattice sites and act as either a donor or an acceptor, characterizing the dopant-site distribution is crucial in understanding the electronic and/or magnetic properties. Conventional diffraction-based methods that are commonly used to determine crystal structures are not able to provide such information due to their limited chemical sensitivity in detecting the very small contribution from the impurities. In addition, phase information cannot be directly measured in a conventional diffraction experiment, adding further difficulties to finding and refining the correct structure. Recent developments in direct x-ray imaging of local structures with atomic resolution, such as x-ray holography[4–7] and tomographic projection using white x-rays,[8] deduce the real-space information from the directional fine structures that are typically 10^{-4} in amplitude of the average background signals, making their applications to dilute systems questionable. Furthermore, x-ray holography is plagued by artifacts that cannot easily be removed for crystalline samples.[9] Thus, except for imaging unit cells of known, simple bulk crystals, no real application has been reported so far.

Here we report a three-dimensional Fourier analysis of ~5% Mn in (Ga,Mn)As thin films using the x-ray standing wave (XSW) technique. (Ga,Mn)As is the most extensively studied prototype of DMS. The ferromagnetic properties of (Ga,Mn)As are mostly governed by the exact placement of Mn in the GaAs unit cell.[3] Unfortunately, the required nonequilibrium growth conditions lead to the distribution of Mn at different lattice sites. Defects such as interstitial Mn (Mn_I), where Mn occupies either the As (Mn_{AsI}) or Ga (Mn_{GaI}) interstitial sites, and antisite As (As_{Ga}) act as double donors.[3] They compensate the holes introduced by the majority of the Mn, which substitutes the Ga (Mn_{Ga}), leading to a lower Curie temperature (T_C). It has been also well recognized that post-growth treatments can have substantial influence on the ferromagnetic properties,[10–13] presumably due to the variation in the defect densities. For example, T_C can be enhanced by low-temperature (LT) annealing while ferromagnetism can be totally suppressed by hydrogenation.[14,15] However, previous investigations[16–22] have provided only limited information about the Mn site distribution.

Using the Fourier components measured by XSW we will present below how real-space images can be reconstructed that allow direct visualization of the atomic distribution of the Mn-dopant atoms in the GaAs unit cells. XSW has shown earlier its strength in precisely locating dilute impurities in solids[23] that occupy a single site and a one-dimensional Fourier analysis has been recently demonstrated.[24] Our atomic-resolution, element-selective x-ray images reveal the complete site occupations of Mn with concentrations as low as 0.3% at each lattice site. These images permit the accurate determination of the dopant site distributions resulting from the specific treatments and their correlation with the electronic properties of the films. The effects of finite Fourier synthesis on the reconstructed images will be discussed with numerical simulations. To reduce the number of structural unknowns in the XSW analysis the samples have been characterized by x-ray diffraction along the specular rod as well and the results will be briefly reported.

II. EXPERIMENTAL DETAILS

The (Ga,Mn)As layer was grown by LT molecular beam epitaxy in a RIBER 32 machine on an Indium-mounted semi-insulating vertical gradient freeze GaAs(001) substrate using a conventional Knudsen cell and a hot-lip effusion cell to provide the Ga and Mn fluxes, respectively. A valved arsenic cracker cell was used in the noncracking mode to supply As_4 with a As_4/Ga beam equivalent pressure ratio of about 10. After thermal deoxidation, a 160-nm-thick GaAs

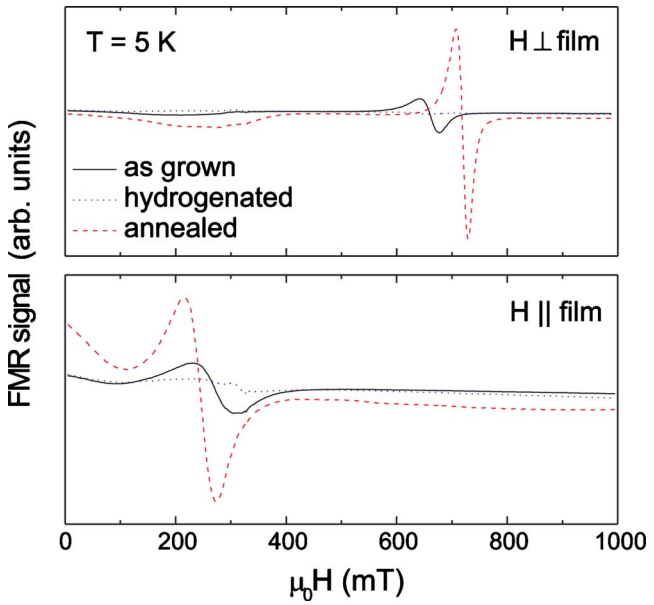

FIG. 1. (Color online) FMR spectra of the as-grown, hydrogenated, and annealed samples measured with the magnetic field **H** normal (upper panel) and parallel (lower panel) to the films.

buffer layer was grown at a substrate temperature T_s of 580 °C. Then the growth was interrupted, the temperature T_{man} of the manipulator was lowered to 275 °C, and, after temperature stabilization, a 23-nm-thick $Ga_{1-x}Mn_xAs$ layer with $x=0.048$ was grown at a growth rate of about 200 nm/h. Extrapolating the relation between T_s and T_{man} from high-to-low temperatures, T_s was estimated to be ~250 °C. Reflection high-energy electron diffraction showed a streaky 1×2 pattern, typical for the (Ga,Mn)As growth, without any indication of a second-phase formation.

After the growth the wafer was cleaved into smaller pieces for annealing at 150 °C in air for 16.5 h or hydrogenation at 170 °C in a remote dc hydrogen plasma operated at 0.9 mbar for two hours. The hole density p and Curie temperature T_c were determined by magnetotransport measurements to be 3.3×10^{20} cm^{-3} and 66 K for the as grown sample and 5.7×10^{20} cm^{-3} and 90 K after annealing. Figure 1 shows the ferromagnetic resonance (FMR) spectra of the as-grown, hydrogenated, and annealed samples measured with a magnetic field normal and parallel to the sample surfaces. All samples exhibited a FMR spectrum typical for the specific preparation. The increase in the FMR intensity and the magnetic anisotropy confirm the improvement of the ferromagnetic properties of the film by annealing whereas the failure to observe FMR in the hydrogenated sample is in accordance with the suppression of ferromagnetism in it. For test purpose additional samples with a thinner film (3 nm $Ga_{0.96}Mn_{0.04}As$) were prepared similarly and characterized by XSW and x-ray diffraction as well.

The x-ray measurements were conducted at beamline ID32 at the European Synchrotron Radiation Facility.[25] Figure 2 shows schematically the experimental setup used for the XSW experiment, where a Si(111) double-crystal monochromator selected the 10 keV undulator radiation, the energy width of which was then further reduced by a Si(555)

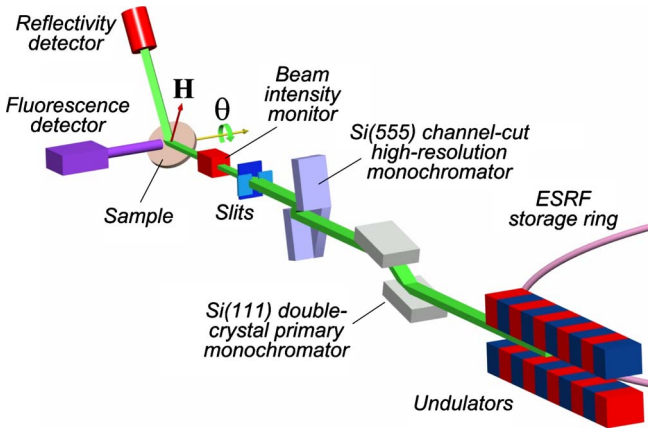

FIG. 2. (Color online) Schematic of the experimental setup for the XSW measurements.

channel-cut crystal to about 15 meV. Together with the small angular spread of the undulator beam, this arrangement allowed the reflectivity curves of GaAs to be properly resolved for all 18 Bragg reflections we used, which were excited individually by aligning the samples on a six-circle diffractometer. At each reflection, specified by a reciprocal lattice vector $\mathbf{h}=(hkl)$, an XSW is formed by superposition of the incident and diffracted x-ray beams. As the incident angle, θ, traverses the range of the reflection, the XSW, which has the periodicity of the Bragg plane spacing d_{hkl}, moves by half of d_{hkl} normal to the Bragg planes. This movement modulates the intensity of the fluorescence x-rays emitted from an element in a fashion that is characteristic of its atomic position. While scanning θ we monitored simultaneously the intensities of the diffracted and the inelastically scattered x-ray photons from the sample.

The extended reflectivity along the specular rod was measured around the GaAs(004) and (002) reflections at photon energies of 10 keV and the Ga K edge (10.369 keV), respectively. The experimental setup was similar to that for the XSW measurements, except the Si(555) channel cut was removed and a plane mirror was used for harmonic rejection.[25] For background subtraction the intensity of diffusely scattered x-rays was also collected along the (001) direction slightly off the specular rod. The Ga K edge was identified by an energy scan of the diffraction anomalous fine structure (DAFS) using the (002) reflection of the 23-nm-thick (Ga,Mn)As film.

III. RESULTS AND ANALYSIS

A. X-ray diffraction: GaAs(004)

Figure 3 shows the extended reflectivity measured along the specular rod around the GaAs(004) reflection for the hydrogenated, as-grown, and annealed samples with the 23-nm-thick (Ga,Mn)As film. After background subtraction the data were compared to the calculated intensity based on the kinematic theory of x-ray diffraction

$$I \propto \exp(-4\mu c_s t/\lambda l - B/2d_l^2)|F_f + F_s|^2/l^2$$

with

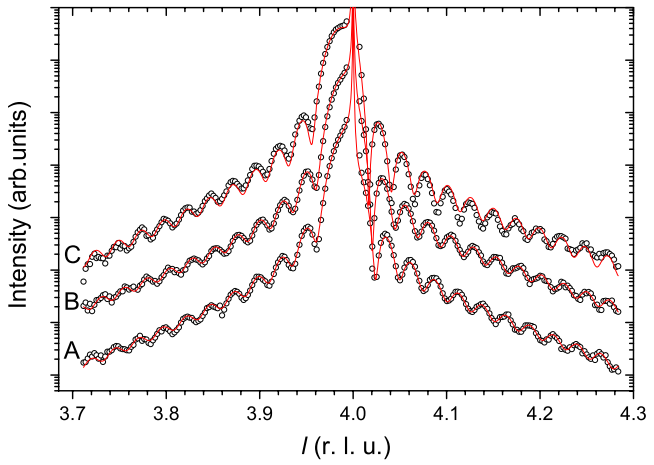

FIG. 3. (Color online) Best fits (red lines) to the measured x-ray specular reflectivity (black circles) around the GaAs(004) reflection for the (A) annealed, (B) as-grown, and (C) hydrogenated samples with the 23-nm-thick films. The data and fits of the different samples are offset for clarity.

$$F_f = \sum_j O_j f_j \exp(2\pi i Z_j l + 2\mu c_s^2 Z_j/\lambda l)$$

and

$$F_s = F_{GaAs}/[1 - \exp(-2\pi i l - 2\mu c_s^2/\lambda l)]. \quad (1)$$

Here l is the momentum transfer along the surface normal direction in reciprocal lattice units of the GaAs substrate. F_f, F_s, and F_{GaAs} are the structure factors of the (Ga,Mn)As film, GaAs substrate and GaAs unit cell, respectively. μ, c_s, and d_l are the linear absorption coefficient, c lattice constant, and (00l) Bragg plane spacing of GaAs. $B=5.9\times10^{-3}$ nm^2 is the isotropic Debye-Waller B factor for GaAs at room temperature.[26] λ and t are the photon wavelength and film thickness. If the jth atom in the film, which has an x-ray scattering factor f_j, is located in the nth unit cell above the (Ga,Mn)As/GaAs interface, its atomic coordinate along the surface normal with the origin chosen to be at the interface can be expressed as $Z_j=(n-1+z)c_f/c_s$, where c_f is the c lattice constant of the film and $z=1/4$, 1/2, 3/4, or 1 depending on whether the atom is Ga or As. O_j is the occupancy of the jth atom and is described by an error function $O_j=\{1-\mathrm{erf}[(c_sZ_j-t)/\sqrt{2}s]\}/2$, where s is the root-mean-square roughness of the surface.

When compared to the data Eq. (1) was multiplied by a linear function (a_1l+a_2) to allow scaling of the intensity to the measured value and to account for any additional l-dependent correction to the intensity resulting from the measurements. In the final curve fitting only five parameters, a_1, a_2, t, c_f, and s were allowed to vary. The best fits to the data are plotted in Fig. 3 and the resulting t, c_f, and s are listed in Table I for the three 23-nm samples. Figure 3 shows that the measured rods are nearly perfectly reproduced by the calculated ones, indicating that the structures of the films are well described by the simple model. Comparable to the earlier reports on thicker films, c_f is found to be slightly larger than c_s (Ref. 27) and to increase further upon hydrogenation.[28] The value of c_f is sensitive not only to the (004) Bragg peak position of the (Ga,Mn)As film at $l\sim3.98$ but also to the location of the intensity minimum at around $l=4.02$, allowing c_f to be precisely determined. Note that the structural model used here does not contain any Mn in the film: it assumes an ideal GaAs substrate and a GaAs overlayer with an elongated c axis. This is justified because for the GaAs(004) reflection all the fcc sublattice sites are equivalent and substituting 5% of the Ga by Mn reduces the structure factor of the film by only about 0.5%. The observed strong interference fringes in Fig. 3 therefore do not arise from an electron density contrast but manifest the small c lattice constant difference between the film and substrate.

Using Eq. (1) we have also analyzed the extended specular reflectivity near the GaAs(004) reflection for the 3-nm-thick (Ga,Mn)As film. The data and best fits are plotted in Fig. 4 and the deduced values of t, c_f, and s are listed in Table I for the hydrogenated, as-grown, and annealed samples.

B. X-ray standing wave imaging

Figure 5 shows as examples the reflectivity curves and the Mn $K\alpha$ fluorescence yields modulated by the GaAs(111), $(1\bar{1}3)$, (004), and (422) XSWs for the annealed sample with the 23-nm-thick film. For a reflection (hkl), the Mn fluorescence yield, Y_{hkl}, induced by the interference field can be described as[29]

TABLE I. Film thickness (t), c lattice constant ratio (c_f/c_s), and surface root-mean-square roughness (s) deduced from the best fits of Eq. (1) to the diffraction data in Figs. 3, 4, and 14 for the 23- and 3-nm-thick films.

Nominal t (nm)	Reflection (hkl)	Sample	t (nm)	c_f/c_s	s (nm)
23		Hydrogenated	23.3	1.0050	0.38
	(004)	As-grown	23.5	1.0039	0.34
		Annealed	22.4	1.0035	0.37
3		Hydrogenated	2.92	1.0098	0.30
	(004)	As-grown	3.46	1.0043	0.43
		Annealed	2.80	1.0041	0.33

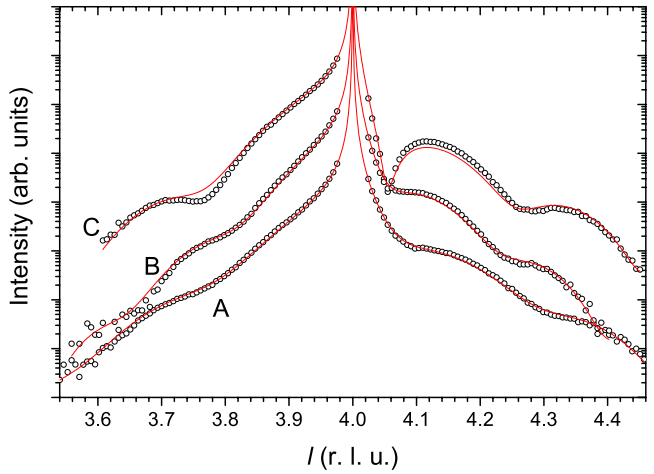

FIG. 4. (Color online) Best fits (red lines) to the measured x-ray specular reflectivity (black circles) around the GaAs(004) reflection for the (A) annealed, (B) as-grown, and (C) hydrogenated samples with the 3-nm-thick films. The data and fits of the different samples are offset for clarity.

$$Y_{hkl}(\theta) \propto 1 + R_{hkl}(\theta) + 2\sqrt{R_{hkl}(\theta)} f_{hkl} \cos(\nu_{hkl}(\theta) - 2\pi P_{hkl}), \tag{2}$$

where $R_{hkl}(\theta)$ is the reflectivity and $\nu_{hkl}(\theta)$ the phase of the XSW. The amplitude and phase of the interference term in Eq. (2), f_{hkl} and P_{hkl}, correspond to the width and center, respectively, of the spatial distribution of the Mn with respect to the Bragg planes of the (hkl) reflection. The distinctive modulations in the Mn yield observed in Fig. 5 result from the movement of the XSWs, which probe the Mn distribution along the different crystallographic directions. With $R_{hkl}(\theta)$ and $\nu_{hkl}(\theta)$ calculated from the dynamical theory of x-ray diffraction,[30] the values of f_{hkl} and P_{hkl} are determined for each reflection by fitting Eq. (2) to the corresponding fluorescence data.

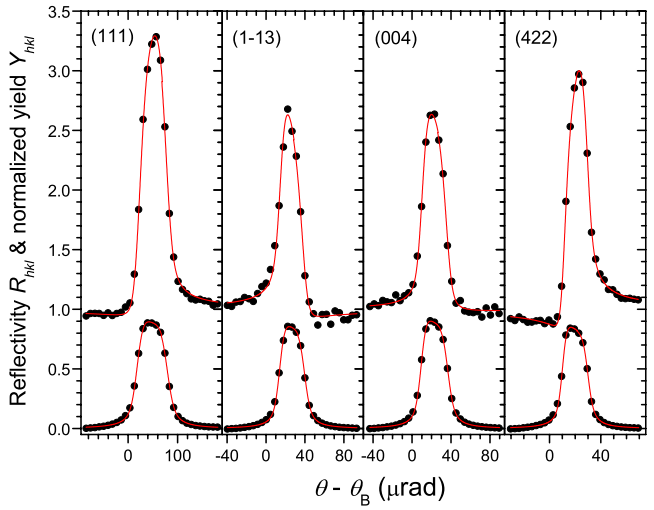

FIG. 5. (Color online) Data (dots) and best fits (red lines) of the reflectivity curves (bottom) and XSW-induced Mn $K\alpha$ fluorescence yields (top) for the GaAs(111), $(1\bar{1}3)$, (004), and (422) reflections for the annealed sample with the 23-nm-thick film.

For the Mn in a (Ga,Mn)As film one can describe its atomic distribution projected to the substrate GaAs unit cell by a Fourier series of $2\pi\mathbf{h}$ as $\rho_a(\mathbf{r}) = (1/V_{uc})\Sigma_{hkl} G_{hkl} \exp(-2\pi i \mathbf{h}\cdot\mathbf{r})$, where $\mathbf{r}$ is a position in the unit cell in units of the lattice constants, V_{uc} the volume of the unit cell, and G_{hkl} the complex coefficient of the $\mathbf{h}$th Fourier component. Since only discrete Bragg reflections are available for the substrate, $\rho_a(\mathbf{r})$ is a periodic function with the periodicity of the substrate lattice. With $\rho_a(\mathbf{r})$ being normalized such that $\int_{V_{uc}} \rho_a(\mathbf{r}) d^3r = 1$, it can be shown that G_{hkl} is related to f_{hkl} and P_{hkl} as $G_{hkl} = f_{hkl} \exp(2\pi i P_{hkl})$. Each XSW measurement thus determines, in contrast to diffraction, not only the amplitude but also the phase of the $\mathbf{h}$th Fourier coefficient of $\rho_a(\mathbf{r})$.[23,29] When f_{hkl} and P_{hkl} are measured for a sufficient number of reflections, $\rho_a(\mathbf{r})$ can be readily reconstructed by the expansion

$$\rho_a(\mathbf{r}) = (1/V_{uc})\left\{1 + 2\sum_{hkl} f_{hkl} \cos[2\pi(P_{hkl} - \mathbf{h}\cdot\mathbf{r})]\right\} \tag{3}$$

considering that $f_{\overline{hkl}} = f_{hkl}$ and $P_{\overline{hkl}} = -P_{hkl}$.

In Figs. 6(a)–6(c) we show the thus reconstructed, *model-independent* three-dimensional images of $\rho_a(\mathbf{r})$ for the Mn in the 23-nm-thick films of the as-grown, annealed, and hydrogenated samples. The reconstructions use the experimentally determined f_{hkl} and P_{hkl} of 18 nonequivalent reflections, which by the crystal symmetry of GaAs amount to 50 Fourier components. For comparison, a ball-and-stick model of GaAs and the corresponding Ga-interstitial (GaI) and As-interstitial (AsI) sites are depicted in Figs. 6(g) and 6(h). The three rendered images in Figs. 6(a)–6(c) show clearly that the majority of the Mn substitutes the Ga, which occupies the corners and face centers of the unit cell. The maxima of the Mn distributions all occur slightly above the bulk Ga site due to the ~0.4% larger c lattice constants of the (Ga,Mn)As layers. The fraction of the Mn at the Ga site, as expressed by the colors of the spots, exhibits a strong dependence on the post-growth treatment. In addition, closer to the center of the unit cell there are eight weaker spots emerging at the locations coinciding with the GaI [cf. Fig. 6(h)] and As [cf. Fig. 6(g)] sites, the intensity of which varies also strongly across the three samples.

It is well known that Fourier synthesis with a limited number of Fourier components may lead to artifacts. To correctly interpret the reconstructed images in Fig. 6 we carried out numerical simulations for the Mn located at the different sublattice sites. We will show below that these artifacts may be easily identified or even removed. The complex coefficient G_{hkl} and thus f_{hkl} and P_{hkl} of the Mn for a given site distribution $\rho_a(\mathbf{r})$ can be calculated by a Fourier expansion as

$$G_{hkl} = \int_{V_{uc}} \rho_a(\mathbf{r}) \exp(2\pi i \mathbf{h}\cdot\mathbf{r}) d^3r = \left(\frac{D_{hkl}}{N}\right) \sum_{j=1}^{4} \left\{ b_j \sum_{k=1}^{N} \exp(2\pi i \mathbf{h}\cdot\mathbf{r}_{jk}) \right\}, \tag{4}$$

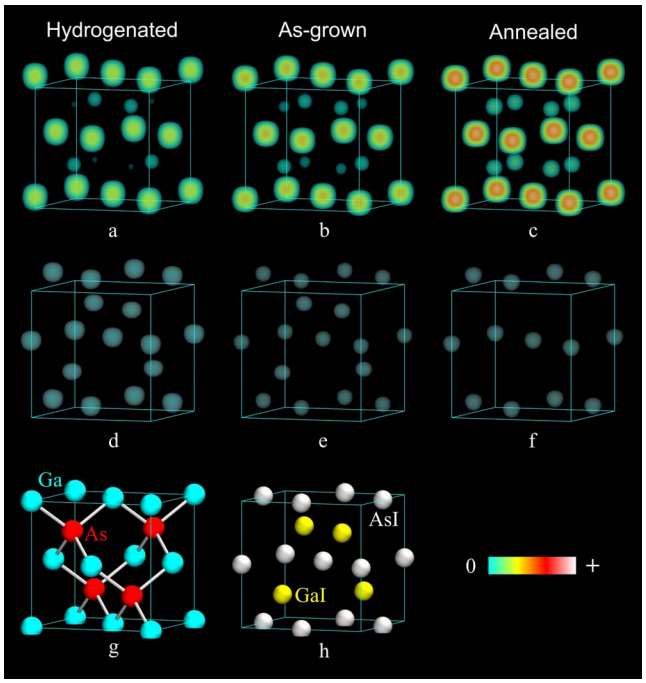

FIG. 6. (Color online) Measured XSW images and model of GaAs lattice sites. [(a)–(c)] Volume-rendered, model-independent images of $\rho_a(\mathbf{r})$ of the 4.8% Mn in the 23-nm-thick (Ga,Mn)As films reconstructed from the 50 Fourier components measured by XSW for the (a) hydrogenated, (b) as-grown, and (c) annealed samples. The site occupation is indicated by the color scale. [(d)–(f)] Images of (a)–(c) after the subtraction of estimated MnGa contributions (see text) for the hydrogenated, as-grown, and annealed samples, respectively. Only the positive parts of the reconstructed $\rho_a(\mathbf{r})$ are shown in the rendered images in (a)–(f). (g) Ball-and-stick model of GaAs. (h) fcc sublattices of GaAs that correspond to the GaI and AsI sites. The blue boxes denote the cubic unit cell of the GaAs substrate.

where j indexes the four fcc sublattices [Figs. 6(g) and 6(h)] and k the N different atomic positions ($\mathbf{r}_{jk}$) associated with each sublattice in the film, b_j is the fraction of the Mn located on sublattice j ($\Sigma b_j \leq 1$), and D_{hkl} is the Debye-Waller factor, which broadens the Mn distribution with a Gaussian function characterized by its in-plane (σ_{ab}) and out-of-plane (σ_c) root-mean-square widths as $D_{hkl}=\exp\{-2\pi^2[\sigma_{ab}^2(h^2+k^2)+\sigma_c^2 l^2]/c_s^2\}$. In the simulations we considered a (Ga,Mn)As layer of a thickness of 40 unit cells with a c lattice constant 0.35% larger than that of pure GaAs (i.e., total-film thickness=22.7 nm). We assumed $\sigma_{ab}=10.7$ pm and $\sigma_c=18.5$ pm for the Mn. For each Mn site distribution the f_{hkl} and P_{hkl} of the same 50 GaAs reflections used in producing Figs. 6(a)–6(c) were calculated from Eq. (4) and then entered into the Fourier expansion in Eq. (3) to obtain $\rho_a(\mathbf{r})$.

Figures 7(a)–7(d) present the result of the simulations where all the Mn is placed on the Ga, AsI, GaI, and As sublattices, respectively. In each case, the brightest spots, representing the maxima of the Mn density $\rho_a(\mathbf{r})$, appear distinctively at the expected fcc site. However, the image also reveals eight weaker spots that are centered at the sites of two other fcc sublattices and are all equally intense. Since no Mn is assigned to these sites in the simulations, these spots are identified to be artifacts arising from the finite number of Fourier components.

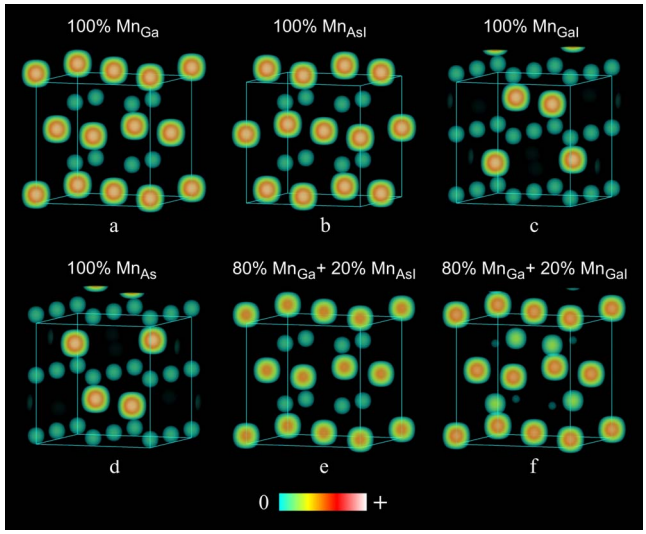

FIG. 7. (Color online) Images of $\rho_a(\mathbf{r})$ simulated for the Mn in a (Ga,Mn)As thin film with different site distributions (see text). Only the positive parts of the reconstructed $\rho_a(\mathbf{r})$ are shown in the images.

In Figs. 7(e) and 7(f) we consider Mn distributions comprising 20% Mn_{AsI} and 20% Mn_{GaI}, respectively. The remaining 80% of the Mn is placed at the Ga site (Mn_{Ga}). Compared to 100% Ga substitution [Fig. 7(a)], moving 20% of the Mn to the GaI sublattice [Fig. 7(f)] weakens the spots at the Ga site. More noticeably, the visibility of the four spots at the GaI site is enhanced at the cost of the four spots at the As site (the opposite effect will occur if the 20% Mn is placed at the As site instead). This intensity contrast between the weak spots at the GaI and As sites in an image can therefore serve as a fingerprint for the presence of Mn_{GaI} or Mn_{As}.

The interpretation becomes less obvious for the case containing 20% Mn_{AsI} [Fig. 7(e)]. Apart from the fact that the spots at the Ga site appear weaker, the image resembles well the 100% Mn_{Ga} case [Fig. 7(a)] but exhibits no features that correspond to the minority site [cf. Fig. 7(b)]. This unexpected appearance originates from systematic omission of specific Fourier components in reconstructing the image, such as all the in-plane reflections in the present case. In the Fourier expansion for the Mn_{Ga}, such omission leads to a negative atomic density at the AsI site, which can fully mask the appearance of the Mn_{AsI} when the majority of the Mn substitutes the Ga. In general, it can be shown that the four fcc sublattice sites are divided into two pairs, (1) Ga and AsI, and (2) As and GaI, such that finite Fourier synthesis of one of the sites may cause negative atomic density at the other site of the same pair. This is also the reason why in Figs. 7(a)–7(d) the weak spots are missing from the sites that are in the same pairs with those occupied by the majority Mn.

When compared to the numerical simulations in Fig. 7, the measured images in Figs. 6(a)–6(c) show clear signs that, in addition to substituting Ga, Mn occupies other positions. In Figs. 6(a) and 6(b), the intensity of Mn_{Ga} is significantly lower than that simulated for 100% Ga substitution. Besides,

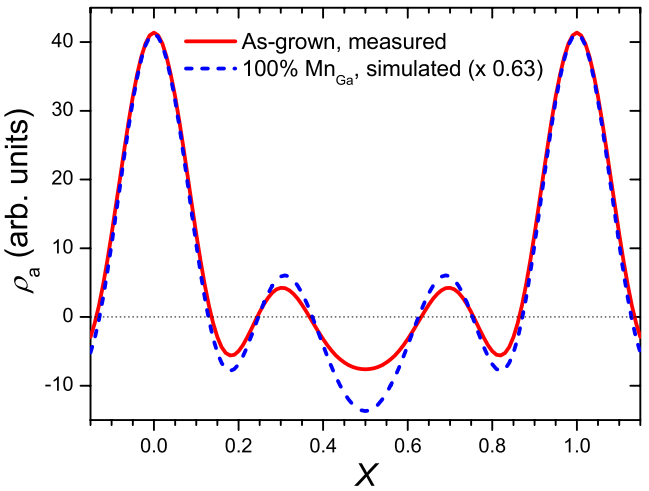

FIG. 8. (Color online) One-dimensional Mn densities $\rho_a(X)$ along one of the unit-cell edges parallel to the sample surface measured from the as-grown sample (red solid line) and simulated for 100% Mn_{Ga} (blue dashed line).

the eight weak spots near the center are not of equal intensity as they should be if they arose merely as artifacts from the finite Fourier expansions: the four spots at the GaI site appear stronger, suggesting the existence of Mn_{GaI}. Furthermore, Mn_{AsI} can be identified by comparing the measured $\rho_a(\mathbf{r})$ to the one calculated for 100% Ga substitution. Such a comparison for the as-grown sample is shown in Fig. 8, where $\rho_a(X)$ represents the one-dimensional Mn density along one of the unit-cell edges parallel to the sample surface. The calculated ρ_a (blue dashed line) has been scaled to have the same values of the measured ρ_a (red solid line) at $X=0$ and 1, where the Mn_{Ga} is located. The figure shows that at $X=0.5$, where Mn_{AsI} could be found, the measured ρ_a is much less negative than the value expected for the 100% Mn_{Ga} case, providing direct evidence for the presence of a significant amount of Mn_{AsI}. Note also that the resolution of the images can be estimated from the full width at the half maximum of the peak at $X=0$ or 1 in Fig. 8 to be 0.09 nm, corresponding closely to the Bragg plane spacing of the highest order reflection used in the XSW measurements, $d_{333}=0.109$ nm.

To visualize the Mn at all minor sites, we subtract from the images in Figs. 6(a)–6(c) the contributions of Mn_{Ga}, which are estimated (Fig. 8) to be 60%, 60%, and 90% of the total Mn, respectively. The resulting images, presented in Figs. 6(d)–6(f), show not only the presence of both Mn_{GaI} and Mn_{AsI} but also the clear dependence of their concentrations on the treatment: they both increase upon hydrogenation whereas the Mn_{GaI} is nearly eliminated by the annealing.

To quantify the Mn site distribution for each sample precisely, a structural model based on Eq. (4) was introduced and refined to best reproduce the 18 measured Fourier components. The thickness, c lattice constant and surface roughness of the film were fixed to the corresponding values listed in Table I and only b_j, σ_{ab}, and σ_c were allowed to vary in the refinement. The best fits to the measured f_{hkl} and P_{hkl} are plotted in Fig. 9, which shows excellent agreement between the calculations and the data. The derived structural parameters are summarized in Figs. 10(a)–10(c), providing the complete Mn distributions with an absolute error estimated to be about ± 0.001 in concentration.

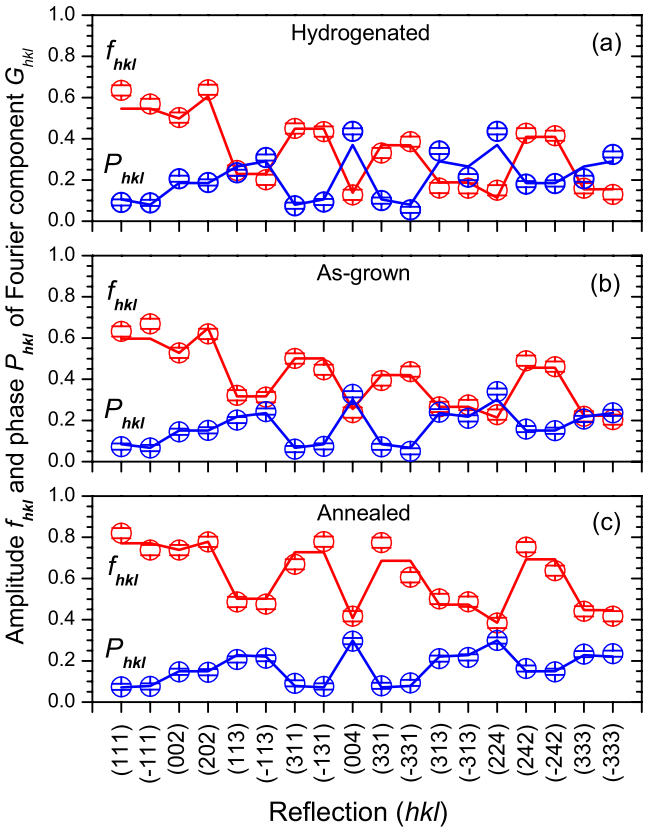

FIG. 9. (Color online) Measured (circles) and refined (lines) phases (P_{hkl}, blue), and amplitudes (f_{hkl}, red) of the 18 Fourier components for the (a) hydrogenated, (b) as-grown, and (c) annealed samples with the 23-nm-thick films.

Using the same XSW analysis we have also determined the Mn-site distribution for the 3-nm-thick $Ga_{0.96}Mn_{0.04}As$ film and studied its dependence on the annealing and hydrogenation. Figure 11 presents the volume-rendered images of ρ_a measured from these samples. The post-growth treatments appear to have much less effects on the Mn distribution for thinner films. For all three samples the eight weak spots closer to the center of the unit cell display nearly identical intensity, indicating the absence of Mn_{As} and Mn_{GaI}. Similar to Fig. 8, the $\rho_a(X)$ measured from the as-grown sample is compared in Fig. 12(a) to that calculated for a 3-nm-thick film with only Mn_{Ga}. The presence of a small amount of Mn_{AsI} is suggested by the slightly less negative value of the measured ρ_a at $X=0.5$. A structural model based on Eq. (4) was refined to determine the Mn-site distributions, taking into account the corresponding values of t, c_f, and s in Table I determined by x-ray diffraction. Figure 12(b) shows as an example that the measured f_{hkl} and P_{hkl} are well reproduced by the refined structural model for the annealed sample. The resulting Mn distributions for the three 3-nm samples are summarized in Figs. 12(c) and 12(d). Compared to the thicker films, the fraction of disordered Mn is much higher and increases upon the post-growth treatments. It is also found that the Mn_{Ga} and Mn_{AsI} are displaced from the ideal

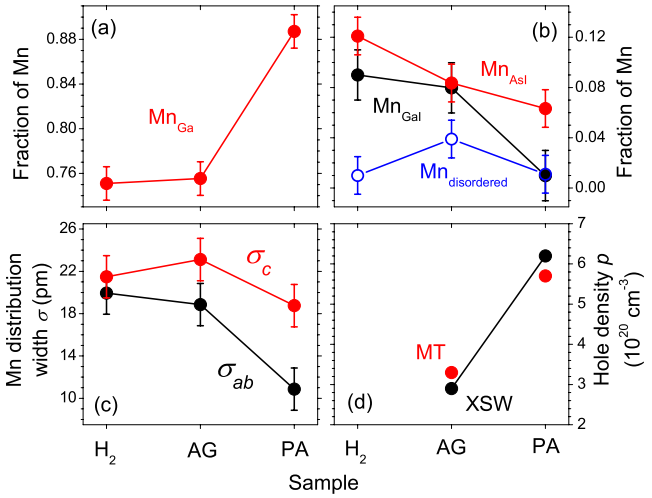

FIG. 10. (Color online) Structural parameters deduced from the XSW analysis and hole densities for the hydrogenated, as-grown, and post-growth annealed samples, labeled as H_2, AG, and PA, respectively, with the 23-nm-thick films. (a) Fraction of the Mn that substitutes Ga, (b) fractions of the Mn that are disordered (blue), at the GaI (black) and AsI sites (red), (c) Mn-distribution widths parallel (σ_{ab}, black) and normal (σ_c, red) to the film, and (d) comparison of the hole densities determined by the magnetotransport measurements (red) and those estimated from the fractions of Mn_{Ga} and Mn_I in (a) and (b) (black) for the as-grown and annealed samples with the 23-nm-thick films.

fcc sublattice sites of the (Ga,Mn)As unit cell by 0.036 nm upwards in all three samples.

C. X-ray anomalous diffraction: GaAs(002)

Contrary to the GaAs(004), the (002) reflection is sensitive to the electron density difference between the Ga and As atomic planes, which are separated by one half of d_{002}, and thus to defects such as As_{Ga}. However, due to the small difference of only two electrons between Ga and As the reflectivity of the (002) reflection is significantly weaker than that of the (004) reflection. Here we explore the possibility of using the extended specular reflectivity near the GaAs(002)

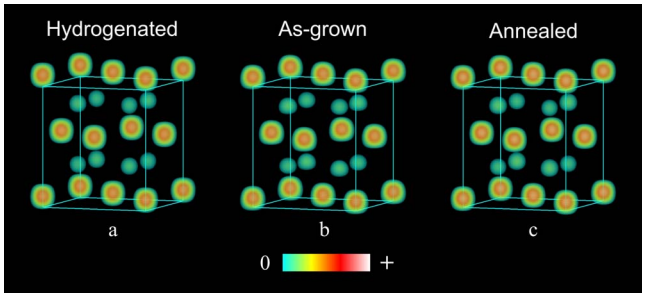

FIG. 11. (Color online) Volume-rendered, model-independent images of $\rho_a(\mathbf{r})$ of the 4% Mn in the 3-nm-thick (Ga,Mn)As films reconstructed from 49 Fourier components measured by XSW for the (a) hydrogenated, (b) as-grown, and (c) annealed samples. The site occupation is indicated by the color scale. Only the positive parts of the reconstructed $\rho_a(\mathbf{r})$ are shown.

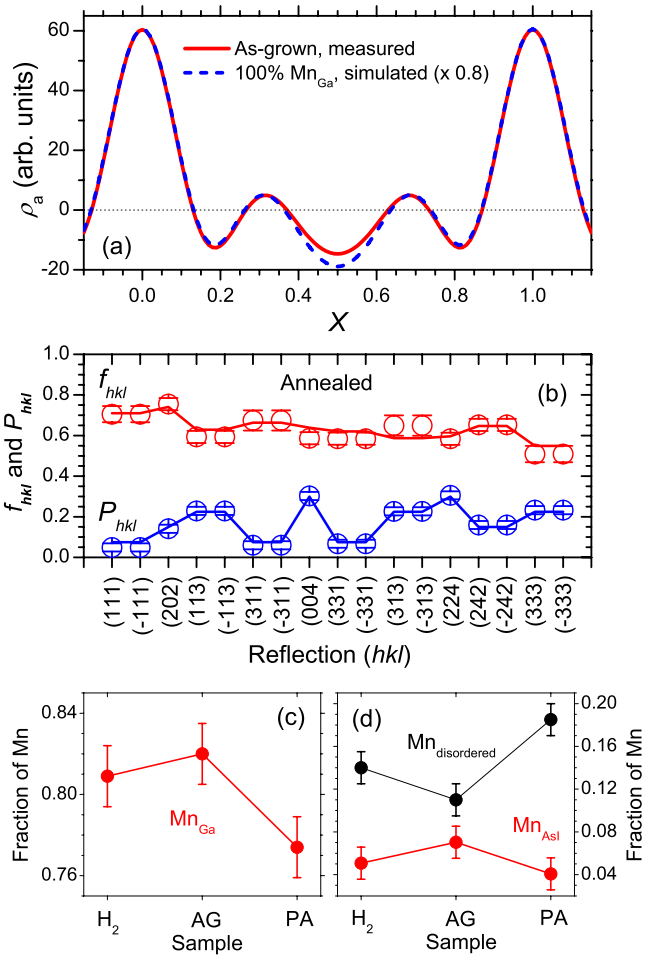

FIG. 12. (Color online) XSW analysis of the 3-nm $Ga_{0.96}Mn_{0.04}As$ samples. (a) Comparison between the $\rho_a(X)$ measured from the as-grown sample (red solid line) and that calculated for a 3-nm-thick film with only Mn_{Ga} (blue dashed line). (b) The measured f_{hkl} and P_{hkl} (opened circles) of 17 reflections and their best fits (solid lines) determined from the model refinement for the annealed sample. [(c) and (d)] The fractions of the Mn_{Ga}, Mn_{AsI}, and disordered Mn in the hydrogenated, as-grown, and post-growth annealed samples, labeled as H_2, AG, and PA, respectively, derived from the model refinement.

reflection under a resonance condition to look for evidence of other defects in the 23-nm-thick (Ga,Mn)As film than those having been identified by XSW.

In Fig. 13(a) the circles represent the integrated peak intensity measured at a fixed $l=1.992$, the center of the (002) reflection of the film, as a function of the incident beam energy for the as-grown sample. Ignoring the small contribution of Mn and other defects, the peak intensity is proportional to $|f_{As}-f_{Ga}|^2=|f_{o,As}+f'_{As}+if''_{As}-f_{o,Ga}-f'_{Ga}-if''_{Ga}|^2$, where f_o denotes the **h**-dependent atomic scattering factor and f' and f'' are the real and imaginary parts, respectively, of the energy-dependent dispersion correction. The 12-fold intensity enhancement observed at the Ga K edge (10.369 keV) arises from the strong reduction in the real part of the Ga scattering factor. To determine the values of f'_{Ga} and f''_{Ga} at the edge we applied the iterative Kramers-Kronig algorithm developed for analyzing DAFS (Ref. 31) to

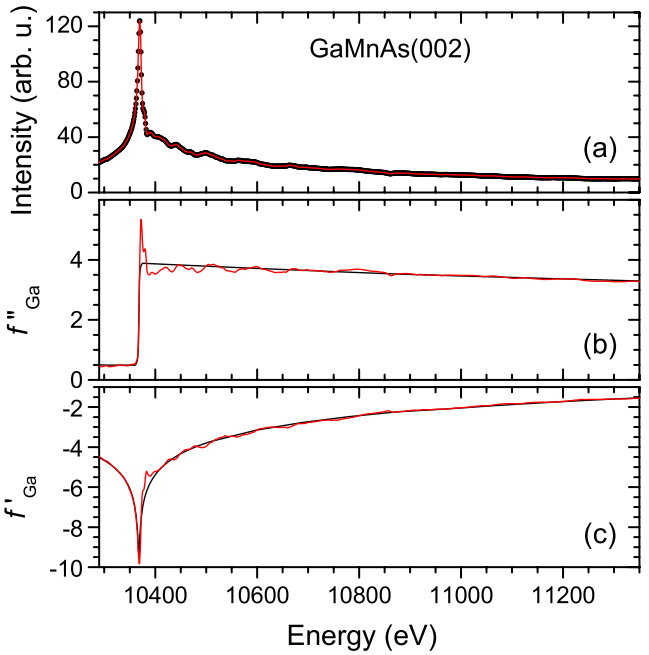

FIG. 13. (Color online) (002) DAFS of the as-grown 23-nm-thick film near the Ga *K* edge (10.369 keV). (a) The peak intensity measured at $l=1.992$ as a function of the incident energy (black circles) and that deduced from the iterative Kramers-Kronig algorithm (red curve). [(b) and (c)] The corresponding f''_{Ga} and f'_{Ga}, respectively, determined by the iterative algorithm (red curves). For comparison, the atomic parts of f''_{Ga} and f'_{Ga} calculated by the Cromer-Liberman method are given as black curves in (b) and (c).

the data in Fig. 13(a). In the algorithm the atomic parts of f''_{Ga} and f'_{Ga} calculated by Sasaki[32] using the Cromer-Liberman method,[33] shown as black curves in Figs. 13(b) and 13(c), respectively, were used in the differential form of the Kramers-Kronig transform. In Figs. 13(b) and 13(c) the red curves represent the thus obtained f''_{Ga} and f'_{Ga}, respectively, which simultaneously satisfy the Kramers-Kronig relation and allow $|f_{\mathrm{As}}-f_{\mathrm{Ga}}|^2$ to reproduce the measured peak intensity in Fig. 13(a).

After locating the Ga *K* edge, we measured the extended specular reflectivity near the GaAs(002) reflection for the as-grown sample at the absorption edge [black curve A in Fig. 14(a)]. Compared to the same measurement repeated at 100 eV below the edge for the same sample [B in Fig. 14(a)], it can be seen that the resonance-induced enhancement of the reflected intensity causes Laue interference fringes to appear on the low-*l* side of the (002) reflection.

In Fig. 14(a) the red curve is the best fit of Eq. (1) to the extended reflectivity measured at the absorption edge considering a_1, a_2, t, c_{f}, and s as free parameters and including the Mn distribution determined by XSW for the 23-nm as-grown sample and the values of f''_{Ga} and f'_{Ga} obtained from Figs. 13(b) and 13(c). The fit not only reproduces unsatisfactorily the amplitudes of the interference fringes but also fails to correctly predict their phases, as highlighted in Fig. 14(b) for $1.7<l<1.86$. Note that this result is not strongly influenced by the values of f'_{Ga} and f''_{Ga} because they are uniform throughout the sample while the phases of the interference fringes near the (002) reflection are mostly determined by the

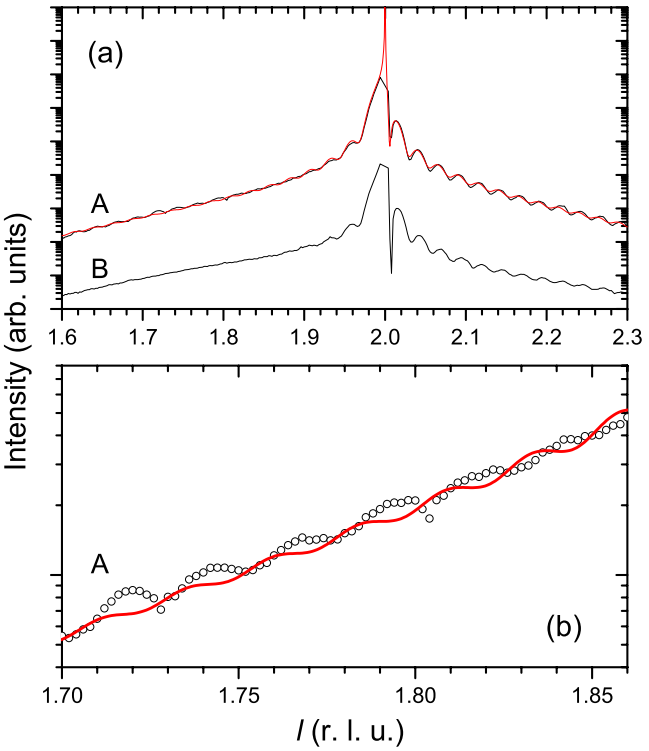

FIG. 14. (Color online) Extended specular reflectivity near the GaAs(002) reflection for the 23-nm-thick as-grown film. (a) Black lines: reflectivity measured at (A) 10.369 and (B) 10.269 keV. Red lines: best fits of Eq. (1) to the black curve A assuming the Mn distributions determined by XSW without additional contributions of other defects (see text). The data and fit are offset for clarity. (b) Closer view of A in (a) over the range $1.7<l<1.86$.

electron density difference between the film and substrate. The disagreement in Fig. 14 therefore supports the presence of additional defects in the as-grown film, such as $\mathrm{As_{Ga}}$, Ga vacancies, and As vacancies, which can alter such electron density contrast. However, we mark that the present anomalous diffraction measurements do not have the sensitivity sufficient for uniquely identifying and quantifying these defects.

IV. DISCUSSION

The Mn distributions determined by XSW for the 23-nm-thick films (Fig. 10) reveals that 16% of the Mn is incorporated in the as-grown sample as interstitial defects, which equally occupy the AsI and GaI sites [Fig. 10(b)]. No other studies have been able to discriminate between the two $\mathrm{Mn_I}$ sites and the total interstitial density that we measure is higher than those reported earlier for similar as-grown samples. For example, previously Rutherford backscattering and particle-induced x-ray emission measurements[16–18] estimated $\mathrm{Mn_I}$ to be about 7% for both a 230-nm ($x=0.05$) and a 21.7-nm ($x=0.07-0.1$) thick as-grown $\mathrm{Ga_{1-x}Mn_xAs}$ film, and detected no $\mathrm{Mn_I}$ for films thinner than ~20 nm ($x=0.07-0.1$). Several cross-sectional scanning tunneling microscopy studies[21,22] reported $\mathrm{As_{Ga}}$ and $\mathrm{Mn_{Ga}}$ densities but failed to identify any interstitial Mn. In fact, $\mathrm{Mn_{GaI}}$ has been

often considered energetically less favorable than Mn_{AsI} in view of their different Coulomb interactions with the nearest neighbors[10,20,34–36] while some calculations suggest similar total energies for the two interstitials.[37] Our analysis provides solid evidence for the presence of Mn_{GaI} in the as-grown film we studied.

Figures 10(a) and 10(b) show that the fraction of Mn_{Ga}, measured to be 75% for the as-grown 23-nm sample, increases after the annealing to 89% at the expense of the Mn_I, mostly the Mn_{GaI}. This is surprising, since it has been commonly assumed that LT annealing does not affect the Mn_{Ga} population[27,38] because of the rather high energy cost for Mn_I to substitute Ga.[3] The increase in Mn_{Ga} upon annealing revealed by the refinement, which is also evident from the images in Fig. 6, could be due to the filling of Ga vacancies, created during either the growth or the annealing process. Figure 10(b) also shows that the 23-nm-thick film contains very small fractions of disordered Mn in all three samples. In contrast, as presented in Figs. 12(c) and 12(d) the as-grown 3-nm-thick film has a three times higher concentration of disordered Mn. After the annealing it increases by another 7% while the sum of Mn_{Ga} and Mn_{AsI} reduces by nearly the same amount. Our observations may be attributed to the presence of a high density of disordered Mn in the oxidized surface layer, which can be further promoted by annealing due to out-diffusion of the near-surface Mn to the surface layer.[10] Hence, for a thicker film or a lower annealing temperature the fraction of disordered Mn is expected to be less.

Using the XSW-determined Mn-site distributions and assuming that each Mn_I compensates two Mn_{Ga}, we estimate in Fig. 10(d) the hole densities for the as-grown and annealed samples, and compare them to those determined by the magnetotransport measurements. Good agreement is achieved with the introduction of 0.4% As_{Ga} acting as double donors, which is consistent with the typical As_{Ga} concentrations reported for LT-grown GaAs.[22,39,40]

In addition to modifying the site distribution, annealing also shows in Fig. 10(c) a strong effect in reducing the Mn-distribution width, in particular, the in-plane component (σ_{ab}), which decreases nearly by half after the treatment to 10.7 pm, very close to the value of $\sqrt{B/8\pi^2}=8.6$ pm for bulk GaAs.[26] This reduction in the Mn Debye-Waller factor contributes partially to the overall increase of the amplitude of ρ_a observed in the image after the annealing [cf. Figs. 6(b) and 6(c)]. We note that the reduction of σ_{ab} after annealing was also observed for the Mn in the 3-nm-thick film. More importantly, Fig. 10(c) reveals essentially no change in either σ_{ab} or σ_c for the Mn upon hydrogenation, offering a new insight into the location of the hydrogen that passivates Mn in (Ga,Mn)As.[28,41] Previous theoretical calculations[42,43] favored a bond-centered configuration over an antibonding one for the hydrogen complexes in (Ga,Mn)As. The calculations predict that the insertion of H at a bond-centered site should displace the Mn away from the Ga site along the Mn-H-As axis[41] and cause significant broadening of the Mn distribution, which is not observed in the present study [Fig. 10(c)]. Our analysis thus supports the antibonding configuration[42,43] or the incorporation of H as an interstitial compensating donor, where in either case hydrogenation has little effect on the Mn-As distance.

V. SUMMARY

Using a sufficient number of element-specific Fourier components determined by the XSW technique, we directly imaged the complete Mn site distributions in (Ga,Mn)As films with concentrations as low as 0.3% at the lattice sites. Structural refinements yielded the site occupation of the Mn with an error in x of about ± 0.001. We demonstrated that the precise information determined by the XSW imaging technique offers the possibility of correlating the structure, growth parameters, and electronic/magnetic properties of a dilute system.

ACKNOWLEDGMENTS

We would like to thank the staff of the ESRF for providing the x-ray beam, and Lionel André, Helena Isern, and Lucien Petit for excellent technical support at the ID32 beamline.

*Present address: Diamond Light Source Ltd, Harwell Science and Innovation Campus, Didcot OX11 0DE, UK; tien-lin.lee@diamond.ac.uk

[1] W. J. Lee, J. Kang, and K. J. Chang, Phys. Rev. B **73**, 024117 (2006).
[2] C. G. Van de Walle and J. Neugebauer, J. Appl. Phys. **95**, 3851 (2004).
[3] T. Jungwirth, J. Sinova, J. Mašek, J. Kučera, and A. H. MacDonald, Rev. Mod. Phys. **78**, 809 (2006).
[4] T. Gog, P. M. Len, G. Materlik, D. Bahr, C. S. Fadley, and C. Sanchez-Hanke, Phys. Rev. Lett. **76**, 3132 (1996).
[5] M. Tegze and G. Faigel, Nature (London) **380**, 49 (1996).
[6] M. Tegze, G. Faigel, S. Marchesini, M. Belakhovsky, and O. Ulrich, Nature (London) **407**, 38 (2000).
[7] K. Hayashi, M. Matsui, Y. Awakura, T. Kaneyoshi, H. Tanida, and M. Ishii, Phys. Rev. B **63**, 041201(R) (2001).
[8] P. Korecki, M. Tolkiehn, D. V. Novikov, G. Materlik, and M. Szymonski, Phys. Rev. Lett. **96**, 035502 (2006).
[9] S. S. Fanchenko, D. V. Novikov, A. Schley, and G. Materlik, Phys. Rev. B **66**, 060104(R) (2002).
[10] K. W. Edmonds, P. Boguslawski, K. Y. Wang, R. P. Campion, S. N. Novikov, N. R. S. Farley, B. L. Gallagher, C. T. Foxon, M. Sawicki, T. Dietl, M. Buongiorno Nardelli, and J. Bernholc, Phys. Rev. Lett. **92**, 037201 (2004).
[11] T. Hayashi, Y. Hashimoto, S. Katsumoto, and Y. Iye, Appl. Phys. Lett. **78**, 1691 (2001).
[12] S. J. Potashnik, K. C. Ku, S. H. Chun, J. J. Berry, N. Samarth, and P. Schiffer, Appl. Phys. Lett. **79**, 1495 (2001).
[13] W. Limmer, A. Koeder, S. Frank, V. Avrutin, W. Schoch, R. Sauer, K. Zuern, J. Eisenmenger, P. Ziemann, E. Peiner, and A. Waag, Phys. Rev. B **71**, 205213 (2005).
[14] S. T. B. Goennenwein, T. A. Wassner, H. Huebl, M. S. Brandt, J.

B. Philipp, M. Opel, R. Gross, A. Koeder, W. Schoch, and A. Waag, Phys. Rev. Lett. **92**, 227202 (2004).
[15] L. Thevenard, L. Largeau, O. Mauguin, A. Lemaître, and B. Theys, Appl. Phys. Lett. **87**, 182506 (2005).
[16] K. M. Yu, W. Walukiewicz, T. Wojtowicz, I. Kuryliszyn, X. Liu, Y. Sasaki, and J. K. Furdyna, Phys. Rev. B **65**, 201303(R) (2002).
[17] K. M. Yu, W. Walukiewicz, T. Wojtowicz, W. L. Lim, X. Liu, U. Bindley, M. Dobrowolska, and J. K. Furdyna, Phys. Rev. B **68**, 041308(R) (2003).
[18] K. M. Yu, W. Walukiewicz, T. Wojtowicz, J. Denlinger, M. A. Scarpulla, X. Liu, and J. K. Furdyna, Appl. Phys. Lett. **86**, 042102 (2005).
[19] V. Holý, Z. Matěj, O. Pacherová, V. Novák, M. Cukr, K. Olejník, and T. Jungwirth, Phys. Rev. B **74**, 245205 (2006).
[20] F. Glas, G. Patriarche, L. Largeau, and A. Lemaître, Phys. Rev. Lett. **93**, 086107 (2004).
[21] A. Mikkelsen, B. Sanyal, J. Sadowski, L. Ouattara, J. Kanski, S. Mirbt, O. Eriksson, and E. Lundgren, Phys. Rev. B **70**, 085411 (2004).
[22] J. N. Gleason, M. E. Hjelmstad, V. D. Dasika, R. S. Goldman, S. Fathpour, S. Charkrabarti, and P. K. Bhattacharya, Appl. Phys. Lett. **86**, 011911 (2005).
[23] N. Hertel, G. Materlik, and J. Zegenhagen, Z. Phys. B **58**, 199 (1985).
[24] L. Cheng, P. Fenter, M. J. Bedzyk, and N. C. Sturchio, Phys. Rev. Lett. **90**, 255503 (2003).
[25] J. Zegenhagen, B. Detlefs, T.-L. Lee, S. Thieß, H. Isern, L. Petit, L. André, J. Roy, Y. Mi, and I. Joumard, J. Electron Spectrosc. Relat. Phenom. **178-179**, 258 (2010).
[26] T. Matsushita and H. Hayashi, Phys. Status Solidi A **41**, 139 (1977).
[27] L. X. Zhao, C. R. Staddon, K. Y. Wang, K. W. Edmonds, R. P. Campion, B. L. Gallagher, and C. T. Foxon, Appl. Phys. Lett. **86**, 071902 (2005).
[28] C. Bihler, G. Ciatto, H. Huebl, G. Martinez-Criado, P. J. Klar, K. Volz, W. Stolz, W. Schoch, W. Limmer, F. Filippone, A. Amore Bonapasta, and M. S. Brandt, Phys. Rev. B **78**, 235208 (2008).
[29] J. Zegenhagen, Surf. Sci. Rep. **18**, 202 (1993).
[30] B. W. Batterman, Phys. Rev. **133**, A759 (1964).
[31] L. B. Sorensen, J. O. Cross, M. Newville, B. Ravel, J. Rehr, H. Stragier, C. Bouldin, and J. C. Woicik, in *Resonant Anomalous X-Ray Scattering: Theory and Applications*, edited by G. Materlik, C. Sparks, and K. Fischer (Elsevier Science B.V., Amsterdam, North Holland, 1994), pp. 389–420.
[32] S. Sasaki, KEK Report **88**, 14 (1989).
[33] D. T. Cromer and D. Liberman, J. Chem. Phys. **53**, 1891 (1970).
[34] S. C. Erwin and A. G. Petukhov, Phys. Rev. Lett. **89**, 227201 (2002).
[35] L. Bergqvist, P. A. Korzhavyi, B. Sanyal, S. Mirbt, I. A. Abrikosov, L. Nordström, E. A. Smirnova, P. Mohn, P. Svedlindh, and O. Eriksson, Phys. Rev. B **67**, 205201 (2003).
[36] P. Mahadevan and A. Zunger, Phys. Rev. B **68**, 075202 (2003).
[37] J. Mašek and F. Máca, Phys. Rev. B **69**, 165212 (2004).
[38] T. Jungwirth, K. Y. Wang, J. Mašek, K. W. Edmonds, J. König, J. Sinova, M. Polini, N. A. Goncharuk, A. H. MacDonald, M. Sawicki, A. W. Rushforth, R. P. Campion, L. X. Zhao, C. T. Foxon, and B. L. Gallagher, Phys. Rev. B **72**, 165204 (2005).
[39] R. M. Feenstra, J. M. Woodall, and G. D. Pettit, Phys. Rev. Lett. **71**, 1176 (1993).
[40] X. Liu, A. Prasad, J. Nishio, E. R. Weber, Z. Liliental-Weber, and W. Walukiewicz, Appl. Phys. Lett. **67**, 279 (1995).
[41] R. Farshchi, D. J. Hwang, N. Misra, C. C. Julaton, K. M. Yu, C. P. Grigoropoulos, and O. D. Dubon, J. Appl. Phys. **106**, 013904 (2009).
[42] J. P. Goss and P. R. Briddon, Phys. Rev. B **72**, 115211 (2005).
[43] A. Amore Bonapasta, F. Filippone, and P. Giannozzi, Phys. Rev. B **72**, 121202(R) (2005).